Check for updates

Enhanced sensitivity in electrochemical detection of ochratoxin A within food samples using ferrocene- and aptamer-tethered gold nanoparticles on disposable electrodes†

Wicem Argoubi, [ID] [a] Faisal K. Algethami [ID] *[b] and Noureddine Raouafi [ID] *[a]

Ensuring food security is crucial for public health, and the presence of mycotoxins, produced by fungi in improperly stored processed or unprocessed food, poses a significant threat. This research introduces a novel approach – a disposable aptasensing platform designed for the detection of ochratoxin A (OTA). The platform employs gold-nanostructured screen-printed carbon electrodes functionalized with a ferrocene derivative, serving as an integrated faradaic transducing system, and an anti-OTA aptamer as a bioreceptor site. Detection relies on the ferrocene electrochemical signal changes induced by the aptamer folding in the presence of the target molecule. Remarkably sensitive, the platform detects OTA within the range of 0.5 to 70 ng mL^{-1} and a detection limit of 11 pg mL^{-1}. This limit is approximately 200 times below the levels stipulated by the European Commission for agricultural commodities. Notably, the sensing device exhibits efficacy in detecting OTA in complex media, such as roasted coffee beans and wine, without the need for sample pretreatment, yielding accurate recoveries. Furthermore, while label-free electrochemical aptasensors have proliferated, this study addresses a gap in understanding the binding mechanisms of some aptasensors. To enhance the experimental findings, a theoretical study was conducted to underscore the specificity of the anti-OTA aptamer as a donor for OTA detection. The molecular docking technique was employed to unveil the key binding region of the aptamer, providing valuable insights into the aptasensor specificity.

Introduction

Diversifying methods beyond antibody-based approaches for highly sensitive detection of analytes of interest is crucial for advancing biochemical analysis.[1] Aptamers, stable single-stranded oligonucleotides selected through the SELEX method, are gaining prominence as superior substitutes to antibodies.[2] Possessing enhanced affinities toward proteins, small molecules, metallic cations and other macromolecular compounds, aptamers opened new avenues in biosensor development for practical applications, including medical diagnostics and the detection of contaminants in food, beverages or the environment.[3–5]

Mycotoxins, such as ochratoxins A, B and C, aflatoxins B1, B2, G1 and G2, *etc.*, produced by *Aspergillus* and *Penicillium*

fungi, pose a threat when present in raw and processed food stored under unfavorable conditions.[6,7] These toxic metabolites are extensively studied due to the mycotoxicosis they induce in humans and animals upon consuming contaminated food and beverages. Among them, OTA has garnered recent attention and has been identified in various products, including cereal-derived items, dried fruits, spices, beer, and wine.[8,9] Regulatory agencies have established maximum toxin levels in food-stuffs to ensure safety. For instance, the European Commission mandates OTA concentrations not exceeding 3 µg kg^{-1} (7.4 nM) for cereal products, 5 µg kg^{-1} (12.4 nM) for roasted coffee, and up to 10 µg kg^{-1} (25 nM) for instant coffee.[10] Wine is subject to even stricter limits, requiring levels below 2 µg kg^{-1} (5 nM) for compliance.[11]

Various standard techniques, such as thin layer chromatography, HPLC,[12] fluorescence spectroscopy, ELISA, *etc.*,[13] are commonly employed to monitor ochratoxin A contamination. Electrochemical methods have gained widespread attention due to their simplicity, cost-effectiveness, ease of operation, high sensitivity, and rapid sensing capabilities.[5,14–18] Indeed, they allow the preparation of sensing devices that fit the World Health Organization "ASSURED: Affordable, Sensitive, Selective, User-friendly, Equipment-free and Deliverable to end-users"

[a]Sensors and Biosensors Group, ACE-Lab (LR99ES15), Faculty of Science, University of Tunis El Manar, 2092 Tunis El Manar, Tunisia. E-mail: noureddine.raouafi@fst.utm.tn

[b]Department of Chemistry, College of Science, Imam Mohammad Ibn Saud Islamic University (IMSIU), P.O. Box 90950, Riyadh 11623, Saudi Arabia. E-mail: falgethami@imamu.edu.sa
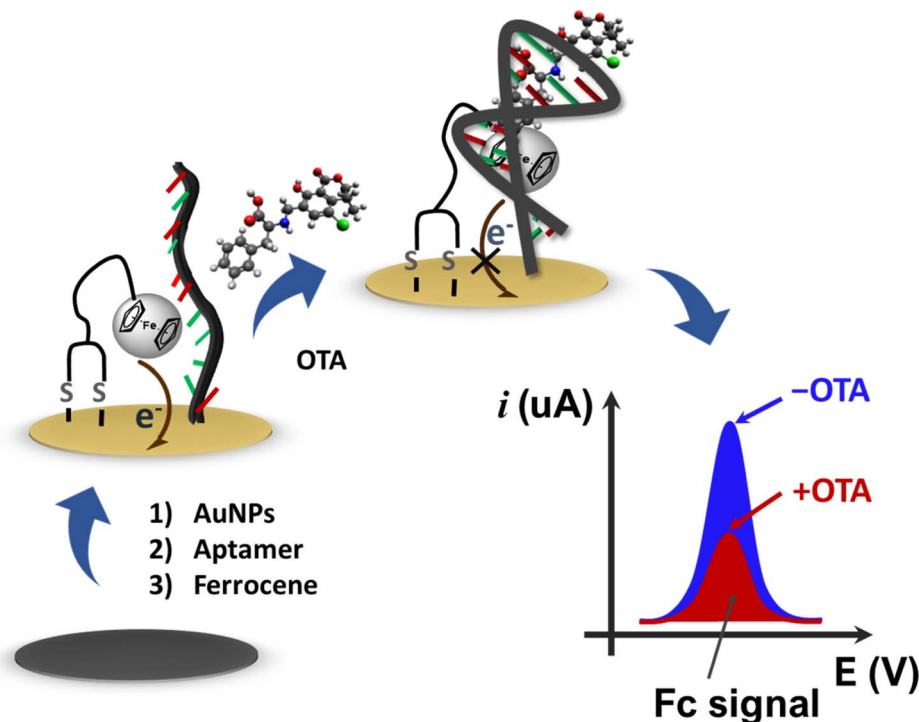
Fig. 1 Schematic sketch of the aptasensor preparation and its use for OTA sensing using differential pulse voltammetry.

criteria.[19,20] For instance, Gökçe et al.[21] developed an aptamer-based electrochemical sensor for OTA detection, demonstrating practical application in samples using pencil graphite electrodes. Rivas et al.[22] presented a label-free electrochemical impedimetric aptasensor for OTA quantitation in cocoa beans. Recently, Hou et al. introduced a novel label-free impedimetric aptasensor employing dual-amplification with Nafion-MWCNTs and Au nanopopcorns for highly selective and ultra-sensitive OTA detection.[23] Dridi et al. reported a differential conducti-metric method for OTA determination using thermolysin embedded in a bovine serum albumin matrix, successfully applied to quantify OTA in spiked olive oil samples.[24]

This paper details the design of a disposable aptasensing platform for OTA using gold nanoparticles-modified screen-printed carbon electrodes. The platform is functionalized with ferrocene as a transducing system and anti-OTA aptamer as a bioreceptor site. Cyclic voltammetry, electrochemical impedance spectroscopy, and SEM imaging were employed to monitor the aptasensor's preparation steps. The developed aptasensor demonstrates efficacy in detecting OTA, with the biosensor's selectivity and specificity evaluated against interference from competitive mycotoxins using various electrochemical techniques. The aptasensor device was successfully applied to determine OTA levels in roasted coffee beans and wine without requiring sample pretreatment. This work introduces a novel platform for highly sensitive detection, utilizing gold nanoparticles anchored to a carbon surface with minimized agglomeration, which in turn yielded a high current response. This innovative approach incorporates a ferrocene-functionalization lipoic acid ester as a transducing agent, enabling an active surface and eliminating the need for external

probes like hexaferrocyanate and ruthenium complexes. Additionally, the study is supported by theoretical research that optimizes and validates the specificity of this detection method, further enhancing its significance.

The principle of the method is depicted in Fig. 1.

Materials and methods

Apparatuses

All electrochemical measurements, including cyclic voltammetry (CV), electrochemical impedance spectroscopy (EIS), and differential pulse voltammetry (DPV), were conducted using a Metrohm-Autolab PGSTAT M204 electrochemical workstation (Utrecht, Netherlands). The acquired data were processed using NOVA v2.13 software. Screen-printed carbon electrodes (SPCEs) on PET sheets, featuring a 3 mm disk as the carbon working electrode, a printed Ag/AgCl reference electrode, and a carbon counter electrode, were employed for the electrochemical experiments. The electrodes were fabricated using a DEK-248 screen printer from DEK International (Weymouth, UK).

For imaging purposes, SEM micrographs and TEM analyses were carried out using a Thermo Fisher Scientific Quanta 650 FEG E-SEM scanning electron microscope (MA, US).

Chemicals and biochemicals

Lipoic acid (99%), ferrocenylmethanol (97%), diméthylaminopyridine (99%), HAuCl$_4 \cdot 3H_2O$ (99%), dicyclohex-ylcarbimide (99%), sodium citrate (99%), mercaptoethanol (99%), phosphate-buffered saline (PBS) tablets, and all solvents were purchased from Sigma-Aldrich (Germany) and used as received without further purification. The 3′-thiolated DNA aptamer (5′-

GAT CGG GTG TGG GTG GGG TAA AGG GAG CAT CGG ACA AAA AAA AAA AAA AAA AAA AAA-C$_6$H$_{12}$-SH-3′),[25] ochratoxin A (OTA), ochratoxin B (OTB), picrotoxin (PIC) were purchased from Isogen Life Science (Spain). The phosphate-buffered saline solution (PBS, pH = 7.4) was prepared by dissolving PBS tablets in deionized water according to the manufacturer recommendations. Tris–EDTA (TE) buffer formed 10 mM TRIS and 1 mM EDTA at pH = 7.5 was used to prepare the aptamer solution. Deionized water, produced using MilliQ system (>18.2 MΩ cm) purchased from Millipore Inc., was used for the preparation of all the solutions.

Preparation of the platform

The synthesis of ferrocenyl lipoic acid ester (FcL) followed established literature procedures.[26–31] Gold nanoparticles with a size of 20 nm were prepared using the Turkevich method.[32] Electrodes underwent an initial cleansing and activation process through 5 voltammetric cycles ranging from 0.0 to +1.5 V in a 0.5 M H$_2$SO$_4$ acidic solution, followed by thorough rinsing with deionized water.

Subsequently, 50 µL of AuNPs was applied to the electrode surface, initiating a two-step nanostructuring process. The first step involved cycling from +0.8 to +1.5 V at a sweep rate of 50 mV s^{-1} to oxidize Au(0) to Au(III). The second step consisted of cycling from +0.8 to 0.0 V at the same sweep rate to reduce Au(III) back to Au(0). This chemical treatment facilitated the adsorption of gold nanoparticles onto the carbon surface.

In a separate solution, 50 µL of a 0.1 M ethanolic solution of FcL was diluted in 450 µL of deionized water to prepare a 10 mM (or 1 mM in the discussion part) FcL solution. The nanostructured electrode was immersed in this solution for several hours to form a dense FcL self-assembled monolayer on the surface of the gold nanoparticles.

The aptamer, dissolved in TE buffer at a concentration of 10 µM, was cast onto the surface of the gold-modified electrode and incubated in a closed container at 4 °C for 16 hours to prevent solvent evaporation. Subsequently, the modified electrode underwent rinsing with deionized water and was immersed for 20 minutes in a 1 mM mercaptoethanol solution. This step served to remove physically adsorbed aptamers and block the bare electrode surface by binding to the gold surface.

Electrochemical measurements

Voltametric measurements were conducted in triplicate by applying 50 µL of a phosphate-buffered saline solution containing the analyte onto the working electrode. CV and DPV curves were recorded at a sweep rate of 50 mV s^{-1} (pulse amplitude: 5 mV and pulse time: 100 ms) within the potential range of −0.1 to +0.4 V. Measurements were taken both before and after sequential additions of 2 µL solutions to achieve OTA concentrations of 0.5, 5, 10, 30, 50, and 70 ng mL^{-1} in PBS.

For the selectivity tests, 10 µL of a 100 ng mL^{-1} solution of OTB and PIC were applied to the biosensor's surface. The DPV current was measured and compared to that obtained for 10 µL of a 30 ng mL^{-1} OTA solution. Specificity was assessed through a comparative analysis of currents obtained for 10 µL solutions containing 30 ng mL^{-1} of OTA and a mixture of OTB (30 ng

mL^{-1}), picrotoxin (100 ng mL^{-1}), and OTA (30 ng mL^{-1}). Chemical structures of OTA, OTB and PIC are given in Fig. S7 from the ESI.†

In silico study

Docking. The *in silico* study involved several steps. Initially, various possible interaction poses between OTA and the aptamer were explored using a docking algorithm. The 3D structure of the aptamer was generated using RNA composer[33] and x3DNA,[34,35] while the 3D structure of OTA was imported from PubChem. After adding polar hydrogen atoms to the aptamer and allowing all bonds to be rotatable for Ochratoxin A, a grid box with a dimension of 66 × 40 × 40 was defined using AutoDock Tools.[36] This grid box was designed to cover the entire aptamer for docking purposes.

The molecular docking between aptamer and OTA was conducted using AutoDock Vina.[37] Subsequently, Discovery Studio Visualizer was used to predict and visualize the interactions between aptamer and OTA.[38]

Molecular dynamics (MD). Then, to confirm the stability of the chosen pose, a MD simulation was carried out with NAMD[39] for 60 ns. Initially, the designed Aptamer–OTA complex was minimized and equilibrated using MD for 10 000 cycles. Detailed MD simulations using the complex structures were conducted with the CHARMM36.[40] The complex is solvated in a cubic box with keeping 10 Å between the complex and the edge of the solvated box. Sodium and chloride ions were added to neutralize the charge of the system. In all simulations the condition was set at the room temperature (310 K) and the atmospheric pressure (1 bar) to closely mimic the general experiment conditions. Subsequently, the fully temperature and pressure equilibrated system was used as the initial configuration for the MD production dynamic analysis. All simulations were conducted using a 2 fs time step.

Data analysis. For a deeply study, the root-mean-square-deviation (RMSD), and radius of gyration (RoG) are calculated with tools implanted in VMD,[41] while the formation of hydrogen bonds (H-bonds) between the aptamer and OTA was analyzed using Pycontact.[42] Free binding energy was also calculated using the MM-PBSA method[43] employing VMD CaFE plugin.[44] It was calculated with 20 snapshots extracted from the trajectories between 40 and 60 ns simulation time (when the system converged). In this method, the binding free energy is decomposed into the relative free energy of the solvated receptor–ligand complex ($\Delta G_{\text{complex,slvd}}$) and the separated, solvated ligand ($\Delta G_{\text{ligand,slvd}}$) and receptor ($\Delta G_{\text{receptor,slvd}}$).

Results and discussion

Preparation of the modified electrodes

TEM and SEM characterizations. To fabricate the device, screen-printed carbon electrodes were initially cleansed using a 0.5 M H$_2$SO$_4$ acidic solution to eliminate adsorbed impurities and activate the surface for efficient absorption of gold nanoparticles. A few cycles, ranging from 0.0 to +1.5 V, were sufficient to achieve a cleaned electrode surface through

electrodeposition.[28] In the subsequent step, cyclic voltammetry was employed to sweep the potential for several cycles between +0.8 and +1.5 V to oxidize gold(0) to gold(III). Then, the potential was cycled from +0.8 to 0.0 V to reduce the oxidized gold atoms back to Au(0). This sequence facilitated the attachment of gold nanoparticles to the electrode surface. Subsequent cyclic voltammetry in sulfuric acid medium revealed two distinctive redox peaks—the first associated with gold oxidation, appearing at approximately +1.2 V and +0.6 V, and the second corresponding to gold oxidation to reduction. These peaks unequivocally confirmed the electrochemical anchoring of gold particles on the carbon surface of the screen-printed electrodes (see ESI Fig. S1†). SEM images provided further validation, depicting nanostructured electrodes with dispersed nanoparticles and some aggregated assemblies.

Following 20 cycles, particulates began forming dense agglomerates (Fig. 2B). In comparison to other methods, such as passive and electrochemical gold salt reduction for depositing gold nanoparticles,[45] this technique has several advantages. These include size homogeneity, high dispersibility into the carbon graphite surface, and stability in the electrochemical response (Table S1 and Fig. S2†). Indeed, drop-casted gold nanoparticles have been observed to being washed out during the stepwise preparation and cleansing of the bioelectrodes.[46] Additionally, the deposited particles from the salt reduction have been shown to form large agglomerates, as demonstrated by Argoubi et al.[28]

Electrochemical characterizations. The FcL/AuNPs/SPCEs underwent further conjugation with the anti-OTA aptamer, followed by coverage with mercaptoethanol to prevent nonspecific adsorption on the gold surface. Cyclic voltammetry revealed successive alterations in the ferrocene redox features upon the addition of the anti-OTA aptamer and mercaptoethanol (Fig. 2C). While the ferrocene signals before and after addition remained similar, a significant decrease in current density was observed. This decrease can be attributed to the formation of an aptamer inhibiting layer, hindering electron transfer, or impeding the diffusion of counter-ions to the inner layer of the electrode surface to compensate for the charge on the ferrocenium cations. Additionally, faradaic impedance spectroscopy demonstrated that the surface modification by gold nanoparticles led to
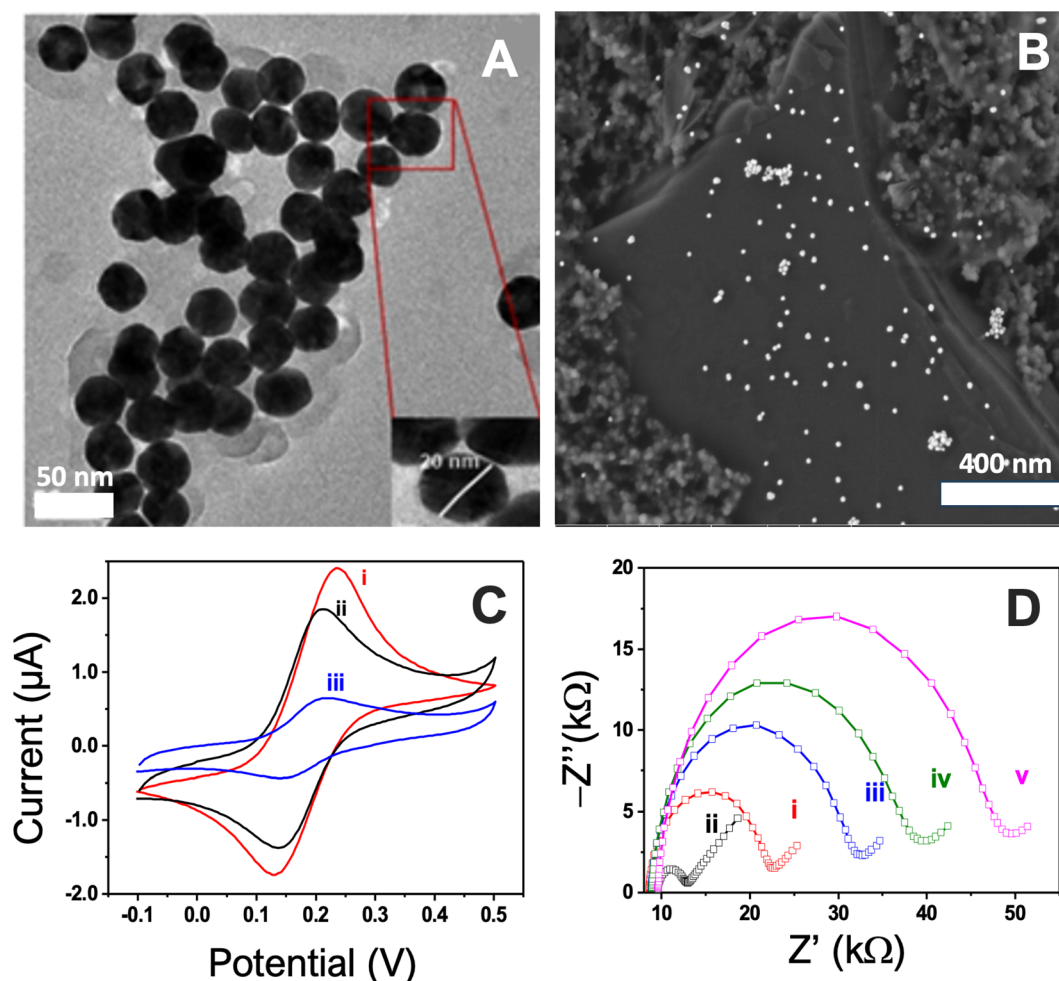

Fig. 2 TEM (A), SEM (B) carbon surface obtained after nanostructuration using 20 cyclic sweeps, (C) CV curves of (i) functionalization of AuNPs by ferrocene derivative, (ii) conjugation with the aptamer, (iii) coverage with mercaptoethanol and (D) stepwise characterization of the surface modification using EIS, (i) bare SPCE, (ii) AuNPs nanostructured electrode, (iii) functionalization of AuNPs by ferrocene derivative, (iv) conjugation with the aptamer, (v) coverage with mercaptoethanol.

a substantial decrease in charge-transfer resistance. This resistance monotonously increased after each step of modification by the ferrocene derivative, the aptamer, and mercaptoethanol due to the formation of a dense non-conductive layer preventing the diffusion of the redox probe to the gold surface (Fig. 2D).

Optimization of the working parameters

Effect of pH in the aptasensor response. The DNA aptamer possesses a sugar-phosphate backbone with multiple nucleobases, and its conformation for capturing OTA is expected to be influenced by the pH of the environment. To comprehensively assess the impact of pH on the performance of the aptasensor, we conducted a systematic study by incubating the aptasensor in TE buffers with varying pH values ranging from 6.0 to 8.5. Subsequently, we measured the corresponding changes in current response (ΔI). The results showed a consistent upward trend in current with increasing pH, peaking at pH 7.5, after which it gradually declined (refer to Fig. 3A). Notably, the pH 7.5 detection solution was selected for subsequent experiments due to its ability to yield the highest current densities. This optimal pH ensures the aptasensor heightened sensitivity and performance in OTA detection.

Effect of incubation time on FcL tethering. Subsequently, the impact of incubation time on the tethering of FcL onto the gold nanoparticle surface was investigated.[47,48] Findings revealed a progressive rise in the current peak associated with ferrocene oxidation as the incubation time increased, reaching a plateau at 120 minutes in a 10 mM FcL solution to form a dense self-assembled layer procuring the highest current densities of the ferrocene oxidation peaks (Fig. 3B). This optimum time frame was employed in subsequent experiments for the electrode functionalization.

Effect of the number of cycles on the current intensity. Employing SEM imaging and coulometric analysis, we investigated the influence of the deposition cycle count on the attachment of gold nanoparticles to the screen-printed carbon electrodes. The number of cycles was systematically adjusted, ranging from 5 to 30 cycles. SEM images depicted in Fig. S2† illustrated a proportional augmentation in the quantity of gold nanoparticles affixed to the surface with an increase in the number of cycles, reaching an optimal level at 20 cycles, as validated by coulometric measurements. This optimal deposition cycle count was employed in subsequent experiments for the electrode functionalization with gold nanoparticles.

Aptasensing of ochratoxin A

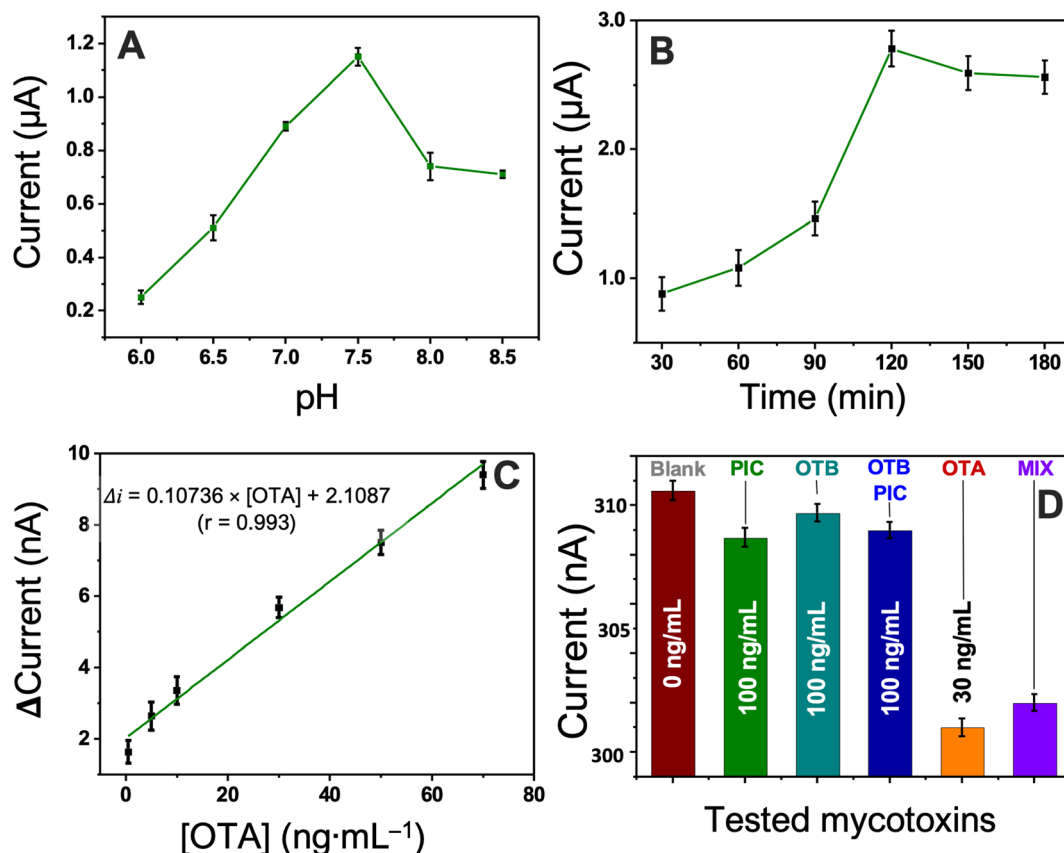The DPV results revealed a proportional decrease in current upon successive additions of OTA aliquots containing known

Fig. 3 (A) Optimization of (A) pH of the working buffer solution and (B) the incubation of FcL, (C) calibration curve for OTA aptasensing in the range of 0.5 to 70 ng mL^{-1}. (D) Selectivity tests in presence of 100 ng mL^{-1} of picrotoxin (PIC), 100 ng mL^{-1} of ochratoxin B (OTA), a mixture of 100 ng mL^{-1} of PIC and 100 ng mL^{-1} of OTB compared to 30 ng mL^{-1} of OTA. MIX bar is related to the electrode challenged with 30 ng mL^{-1} of OTA, 100 ng mL^{-1} of OTB and 100 ng mL^{-1} of PIC.

concentrations of the analyte to the device. This phenomenon can be attributed to the blocking effect arising from the formation of a biocomplex between the Aptamer and OTA, as illustrated in the DPV curves presented in Fig. S3.†

The linear regression equation was fitted to ΔI (nA) = $0.10736 \times$ [OTA] (ng mL^{-1}) + 2.1087 ($r = 0.993$) (Fig. 3C). The estimated limits of detection and quantification were determined as 11 and 33 pg mL^{-1}, respectively. These values were calculated based on the concentration of toxin corresponding to the 3.3 and 10 times "s/m" ratio, where "s" represents the standard deviation of the blank signal (three replicates), and "m" denotes the slope of the related calibration curve. The linear range spans from 0.5 to 70 ng mL^{-1}, with a limit of detection of 11 pg mL^{-1}. Importantly, this range encompasses the authorized levels of OTA in various commodities such as cereal-processed goods and beverages like wine and grape juice. Furthermore, the limit of detection is approximately 180 times below the lowest permissible limit, underscoring the utility of this method for accurately determining OTA levels in widely consumed products.

Selectivity of OTA aptasensor

In assessing the selectivity of OTA detection for practical implementation, we compared the current variations induced by other mycotoxins, namely ochratoxin B and picrotoxin (Fig. S7†). As depicted in Fig. 3D (DPV curves are given in Fig. S5†), the changes in current intensity induced by these two mycotoxins were minimal, even at concentrations three times higher than that of the target mycotoxin. For the specificity test, we introduced a mixture of OTB and picrotoxin followed by a mixture of OTA, OTB, and picrotoxin to the aptasensor. Interestingly, only the latter mixture induced a significant current drop, indicating a high specificity of the sensing platform for OTA. Despite the structural similarity between OTA and OTB, the latter did not interfere with the aptasensor response. This ability to distinguish between them is crucial for the selectivity of the aptasensing platform.

Comparison with literature

While more sensitive electrochemical approaches for ochratoxin A detection, such as those involving methylene blue (MB)

Table 2 Recovery results from analysis of OTA in grounded coffee beans and French wine samples

Samples	Detected (D)	Added (A)	Detected after addition (R)	% Recovery $100 \times (R - D)/A$
Wine	1.10	5.00	6.46	107.20 ± 3.60
		10.00	11.90	108.00 ± 3.20
Coffee	11.40	5	16.27	97.40 ± 2.40
		10	21.12	97.20 ± 2.85

intercalation,[49] a fluorescent aptamer-based biosensor utilizing a cascade strand displacement reaction,[50] polythionine and IrO$_2$ nanoparticles[22] or DNAzyme/aptamer and enzymatic reading[51] have been recently reported, our aptasensing platform offers notable analytical advantages. The current approach attains an exceptionally low limit of detection without the need for amplification or the intercalation of redox species into the DNA structure or using carbonaceous nanomaterials. This achievement is made possible by leveraging a novel nanostructured faradaic platform. Consequently, our approach is simpler and more cost-effective, providing a wide range of response and one of the lowest reported detection limits for differential pulse voltammetry with ferrocene labeling in OTA detection (Table 1).

Determination of OTA levels in real samples

To assess the practical reliability of the proposed sensing system, the aptasensor was employed to determine the recoveries of five different OTA concentrations using standard addition methods in ground coffee beans and French wine samples[9] (DPV curves are given in Fig. S6†). The results, as presented in Table 2, reveal recoveries within the range of 97.4–97.2% and 107.2–108.0% respectively for the two samples. These findings affirm that the proposed sensing system is suitable for the analysis of OTA in agricultural commodities. The aptasensor's robust performance in the quantitative determination of mycotoxins in food samples, without the need for sample pretreatment or concentration, holds significant promise for enhancing quality control in food safety. The system provides a simple, rapid, and sensitive testing solution for monitoring mycotoxins in agricultural products.

Table 1 Comparison of the performances of the developed aptasensing platform with similar aptasensors from literature

| Platform	Detection technique	Linear range (ng mL^{-1})	LoD (ng mL^{-1})	Ref.
SPCE, oxidation of amines using HDMA and MB tagged anti-OTA	DPV	0.01–5.0	0.01	49
OTA@AP@MBs/cDNA cascade strand displacement reaction	FL	1–2000	0.63	50
Single-walled carbon nanohorns	FL	8.0–200.0	6.80	52
Aptamer/AuNPs	Colorimetry	0.5–6.0	0.4	53
Aptamer/Au@Fe$_3$O$_4$NPs	Colorimetry	0.5–100	0.03	54
Aptamer/DNAzyme/Fe$_3$O$_4$NPs/glucometer	Amperometry	0.001–250	0.11	51
Aptamer/thionine-IrO$_2$NPs/SPCE	EIS	0.005–40	0.005	22
Aptamer/diazonium/SPCE	EIS	0.15–2.5	0.15	55
Aptamer/FcL/AuNPs/SPCE	DPV	0.5–70	0.011	This work
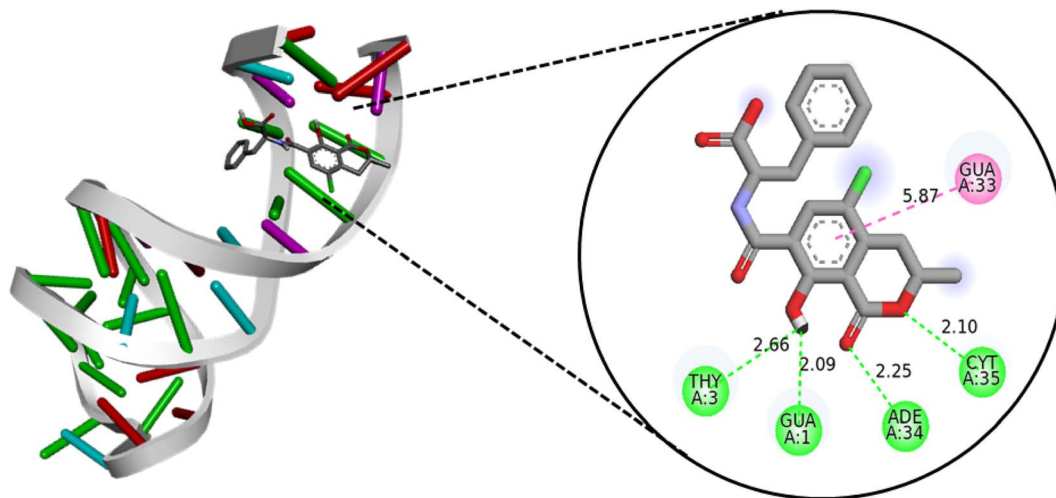
Fig. 4 Interaction of ochratoxin A with the aptamer obtained by docking using Vina software visualized with Discovery Studio.

In silico study

In silico simulations, by molecular docking and molecular dynamics, can provide several useful information on the binding site, the interaction energies and study degradation kinetics,[56–60] especially if coupled to experimental techniques.[57,61]

Docking results. The aptamer–ochratoxin complex with the lowest energy score, as determined by the docking software, was chosen as the optimal conformation. Docking results, detailed in Table S2,† indicate a top score of -9.0 kcal mol^{-1} (-37.65 kJ mol^{-1}), with corresponding interactions depicted in Fig. 4. OTA primarily interacts with five nucleotides of the aptamer, forming four hydrogen bonds with GUA1, THY3, ADE34, CYT35, and one hydrophobic interaction with GUA33 through π–π stacking.
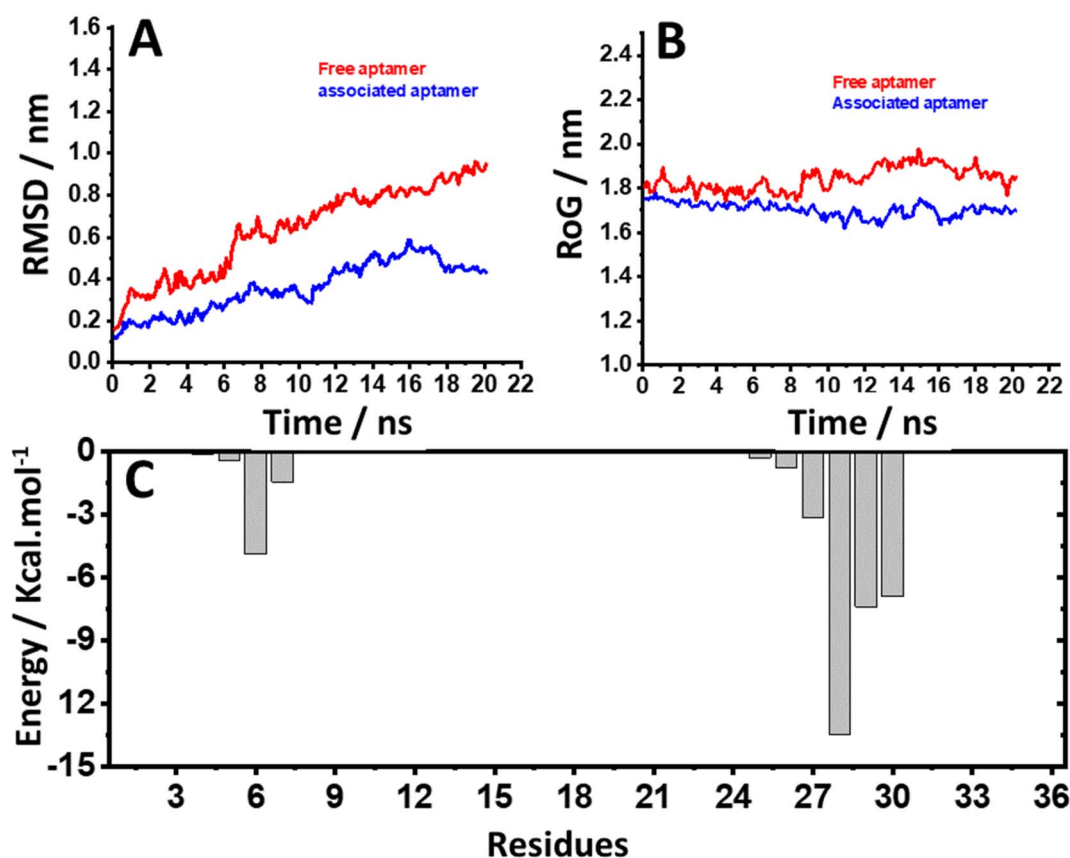

Fig. 5 Time-dependent RMSD (A) and RoG (B) plots for the associated and the free aptamer for the last 20 ns of the simulation time. Per-residue contribution plot for the aptamer in mechanics energy (C).

Analysis of the MD results. To validate the reliability of these results, a MD simulation of the aptamer–OTA complex was conducted for a minimum of 60 ns using the same MD procedure. The RMSD of the aptamer associated with OTA and the free aptamer was calculated in the last 20 ns and is illustrated in Fig. 5A. The average RMSD of the associated aptamer exhibited a significant 56% decrease compared to the RMSD average of the free aptamer, indicating a stabilization of the aptamer upon association with OTA through non-bonded interactions.

Furthermore, the RoG results, as depicted in Fig. 5B, align with the RMSD analysis, indicating that the associated aptamer is more stable than the free one, and the system has achieved convergence. To better understand this stability, an analysis of hydrogen bond interactions between the ligand and the receptor was conducted. The results indicate that OTA primarily interacts with six nucleotides from the aptamer – GUA1, ADE2, THY3, GUA25, ADE26, and ADE34 – with a frequency of occupancy exceeding 50% throughout the simulation time (Table S3†). These findings are consistent with the docking results, confirming the stability of the interaction pose between the aptamer and OTA.

Further analysis reveals that CYT28, ADE29, and THY30 nucleotides from the aptamer play significant roles in the mechanical energy (ΔE_{elec} and ΔE_{VdW}), as illustrated in Fig. 5C. The calculated free energy for the solvated complex formed by the association of the aptamer and OTA is -9.22 kcal mol^{-1}, with a substantial contribution from ΔE_{elec} and ΔE_{VdW}. To comprehend the effect of different energy contribution terms, the results are detailed in Table S4.†

These results enable the prediction of interaction poses and identify residues involved in non-bonded interactions with OTA. The affinity and stability of the formed complex can be reliably predicted using these findings. The free binding energy further confirms the system's convergence, supported by reasonable values of RMSD and RoG. The stability observed is attributed to the formation of hydrogen bonds between the ligand and six nucleotides from the aptamer, along with three electrostatic interactions with three different nucleotides from the aptamer.

Conclusion

This study presents a straightforward design for an aptasensing device targeting ochratoxin A, employing gold nanoparticles, a ferrocene derivative, and an anti-OTA aptamer. The platform capitalizes on the alterations in the ferrocene signal induced by the folding of the aptamer in the presence of OTA, which avoid using hexacyanoferrate or ruthenium complexes for signal transduction. The device exhibits remarkable sensitivity, detecting OTA within the range of 0.5 to 70 ng mL^{-1}, with a limit of detection of 11 pg mL^{-1}. This detection limit falls below the threshold levels established by the EC for agricultural commodities. The aptasensing device was successfully applied to quantify OTA in complex untreated media, specifically coffee beans, and French wine, achieving good recoveries (97.20 ± 2.85 and 108.00 ± 3.20) without the need for sample pretreatment. Additionally, an *in silico* evaluation, encompassing

structural similarity, molecular docking, and molecular dynamics, was conducted to unveil the key binding region of the OTA aptamer through molecular docking technology.

Data availability

Data will be made available on request.

Conflicts of interest

The authors declare no conflict of interest.

Acknowledgements

References

1 G. Atik, N. M. Kilic, N. Horzum, D. Odaci and S. Timur, *ACS Appl. Mater. Interfaces*, 2023, **15**, 24109–24119.

2 S. Liu, F. Zhao, K. Xu, M. Cao, M. Sohail, B. Li and X. Zhang, *Anal. Chim. Acta*, 2023, 342044.

3 K. Y. Goud, K. K. Reddy, M. Satyanarayana, S. Kummari and K. V. Gobi, *Microchim. Acta*, 2019, **187**, 29.

4 F. K. Algethami, A. Rabti, M. Mastouri, S. Ben Aoun, B. Y. Abdulkhair and N. Raouafi, *Talanta*, 2023, **258**, 124445.

5 F. Algethami, A. Rabti, M. Mastouri, B. Abdulkhair, S. Ben Aoun and N. Raouafi, *RSC Adv.*, 2023, **13**, 21336–21344.

6 R. A. El-Sayed, A. B. Jebur, W. Kang and F. M. El-Demerdash, *J. Future Foods*, 2022, **2**, 91–102.

7 S. Ben Aissa, R. K. Mishra, N. Raouafi and J. L. Marty, in *Nanosensors*, CRC Press, 2023, p. 205.

8 L. Wang, Q. Wang, S. Wang, R. Cai, Y. Yuan, T. Yue and Z. Wang, *Curr. Res. Food Sci.*, 2022, **5**, 1539–1549.

9 N. Mejri-Omrani, A. Miodek, B. Zribi, M. Marrakchi, M. Hamdi, J.-L. Marty and H. Korri-Youssoufi, *Anal. Chim. Acta*, 2016, **920**, 37–46.

10 I. M. Hwang, J. Y. Jeong, B. Park, J. Y. Choi, N. Khan, N. Jamila, B. R. Yoon and J. S. Kim, *Food Addit. Contam., Part A: Chem., Anal., Control, Exposure Risk Assess.*, 2023, **40**, 1275–1284.

11 W. Chtioui, S. Heleno, Q. Migheli and P. Rodrigues, *Int. J. Food Microbiol.*, 2023, **407**, 110425.

12 F. Kardani, A. Z. Jelyani, M. Rashedinia, S. Shariati, M. Hashemi, S. M. A. Noori and M. Mahdavinia, *Food Chemistry Advances*, 2023, **3**, 100490.

13 J. Zhang, D. Xu, Y. Zhang, Z. Luo, Y. Zhao, X. Zheng, H. Yang and Y. Zhou, *Spectrochim. Acta, Part A*, 2024, **304**, 123312.

14 M. Zouari, S. Campuzano, J. Pingarrón and N. Raouafi, *Biosens. Bioelectron.*, 2017, **91**, 40–45.

15 F. K. Algethami, A. Rabti, M. Mastouri, S. Ben Aoun, L. S. Alqarni, M. R. Elamin and N. Raouafi, *Microchim. Acta*, 2023, **190**, 434.

16 S. Baachaoui, M. Mastouri, M. Meftah, B. Yaacoubi-Loueslati and N. Raouafi, *Biosensors*, 2023, **13**, 240.

17 S. Baachaoui, W. Mabrouk, K. Charradi, B. Slimi, A. M. Ramadan, R. M. I. Elsamra, A. Alhussein, S. M. A. S. Keshk and N. Raouafi, *R. Soc. Open Sci.*, 2023, **10**, 230294.

18 B. Ouedraogo, S. Baachaoui, A. Tall, I. Tapsoba and N. Raouafi, *Microchim. Acta*, 2023, **190**, 316.

19 S. Smith, J. G. Korvink, D. Mager and K. Land, *RSC Adv.*, 2018, **8**, 34012–34034.

20 J. A. Otoo and T. S. Schlappi, *Biosensors*, 2022, **12**, 124.

21 G. Gökçe, S. B. Aissa, K. Nemčeková, G. Catanante, N. Raouafi and J.-L. Marty, *Food Control*, 2020, **115**, 107271.

22 L. Rivas, C. C. Mayorga-Martinez, D. Quesada-González, A. Zamora-Gálvez, A. de la Escosura-Muñiz and A. Merkoçi, *Anal. Chem.*, 2015, **87**, 5167–5172.

23 Y. Hou, N. Long, Q. Xu, Y. Li, P. Song, M. Yang, J. Wang, L. Zhou, P. Sheng and W. Kong, *Food Chem.*, 2023, **403**, 134375.

24 F. Dridi, M. Marrakchi, M. Gargouri, J. Saulnier, N. Jaffrezic-Renault and F. Lagarde, *Anal. Methods*, 2015, **7**, 8954–8960.

25 L. Barthelmebs, J. Jonca, A. Hayat, B. Prieto-Simon and J.-L. Marty, *Food Control*, 2011, **22**, 737–743.

26 A. Mars, C. Parolo, N. Raouafi, K. Boujlel and A. Merkoçi, *J. Mater. Chem. B*, 2013, **1**, 2951–2955.

27 A. Mars, C. Parolo, A. de la Escosura-Muñiz, N. Raouafi and A. Merkoçi, *Electroanalysis*, 2016, **28**, 1795–1802.

28 W. Argoubi, M. Saadaoui, S. Ben Aoun and N. Raouafi, *Beilstein J. Nanotechnol.*, 2015, **6**, 1840–1852.

29 M. Li, L.-Q. Jiang, L. Lin, Y.-F. Li, D.-L. Yu, L.-L. Cui and X.-Q. He, *J. Solid State Electrochem.*, 2014, **18**, 2743–2753.

30 M. Zouari, S. Campuzano, J. Pingarrón and N. Raouafi, *Electrochim. Acta*, 2018, **262**, 39–47.

31 E. Vargas, E. Povedano, V. Montiel, R. Torrente-Rodriguez, M. Zouari, J. Montoya, N. Raouafi, S. Campuzano and J. Pingarron, *Sensors*, 2018, **18**, 863.

32 J. Kimling, M. Maier, B. Okenve, V. Kotaidis, H. Ballot and A. Plech, *J. Phys. Chem. B*, 2006, **110**, 15700–15707.

33 M. Antczak, M. Popenda, T. Zok, J. Sarzynska, T. Ratajczak, K. Tomczyk, R. W. Adamiak and M. Szachniuk, *Acta Biochim. Pol.*, 2016, **63**(4), 737–744.

34 S. Li, W. K. Olson and X.-J. Lu, *Nucleic Acids Res.*, 2019, **47**(W1), W26–W34.

35 X.-J. Lu and W. K. Olson, *Nat. Protoc.*, 2008, **3**, 1213–1227.

36 G. M. Morris, R. Huey, W. Lindstrom, M. F. Sanner, R. K. Belew, D. S. Goodsell and A. J. Olson, *J. Comput. Chem.*, 2009, **30**(16), 2785–2791.

37 J. Eberhardt, D. Santos-Martins, A. F. Tillack and S. Forli, *J. Chem. Inf. Model.*, 2021, **61**, 3891–3898.

38 *BIOVIA Discovery Studio Visualizer*, **https://discover.3ds.com/ discovery-studio-visualizer-download**.

39 J. C. Phillips, D. J. Hardy, J. D. C. Maia, J. E. Stone, J. V. Ribeiro, R. C. Bernardi, R. Buch, G. Fiorin, J. Hénin,

W. Jiang, R. McGreevy, M. C. R. Melo, B. K. Radak, R. D. Skeel, A. Singharoy, Y. Wang, B. Roux, A. Aksimentiev, Z. Luthey-Schulten, L. V. Kalé, K. Schulten, C. Chipot and E. Tajkhorshid, *J. Chem. Phys.*, 2020, **153**(4), 044130.

40 J. Huang and A. D. MacKerell, *J. Comput. Chem.*, 2013, **34**(25), 2135–2145.

41 W. Humphrey, A. Dalke and K. Schulten, *J. Mol. Graphics*, 1996, **14**(1), 33–38.

42 M. Scheurer, P. Rodenkirch, M. Siggel, R. C. Bernardi, K. Schulten, E. Tajkhorshid and T. Rudack, *Biophys. J.*, 2018, **114**(3), 577–583.

43 B. R. I. Miller, T. D. Jr. McGee, J. M. Swails, N. Homeyer, H. Gohlke and A. E. Roitberg, *J. Chem. Theory Comput.*, 2012, **8**, 3314–3321.

44 H. Liu and T. Hou, *Bioinformatics*, 2016, **32**(14), 2216–2218.

45 D. Antuña-Jiménez, M. B. González-García, D. Hernández-Santos and P. Fanjul-Bolado, *Biosensors*, 2020, **10**, 9.

46 J. T. Steven, V. B. Golovko, B. Johannessen and A. T. Marshall, *Electrochim. Acta*, 2016, **187**, 593–604.

47 R. Sahli, C. Fave, N. Raouafi, K. Boujlel, B. Schöllhorn and B. Limoges, *Langmuir*, 2013, **29**, 5360–5368.

48 M. Hamami, N. Raouafi and H. Korri-Youssoufi, *Appl. Sci.*, 2021, **11**, 1382.

49 G. Catanante, R. K. Mishra, A. Hayat and J.-L. Marty, *Talanta*, 2016, **153**, 138–144.

50 B. Han, C. Fang, L. Sha, M. Jalalah, M. S. Al-Assiri, F. A. Harraz and Y. Cao, *Food Chem.*, 2021, **338**, 127827.

51 S. Zhang, Y. Luan, M. Xiong, J. Zhang, R. Lake and Y. Lu, *ACS Appl. Mater. Interfaces*, 2021, **13**, 9472–9481.

52 L. Lv, C. Cui, C. Liang, W. Quan, S. Wang and Z. Guo, *Food Control*, 2016, **60**, 296–301.

53 C. Yang, Y. Wang, J.-L. Marty and X. Yang, *Biosens. Bioelectron.*, 2011, **26**, 2724–2727.

54 C. Wang, J. Qian, K. Wang, X. Yang, Q. Liu, N. Hao, C. Wang, X. Dong and X. Huang, *Biosens. Bioelectron.*, 2016, **77**, 1183–1191.

55 R. K. Mishra, A. Hayat, G. Catanante, C. Ocaña and J.-L. Marty, *Anal. Chim. Acta*, 2015, **889**, 106–112.

56 S. J. Lee, J. Cho, B.-H. Lee, D. Hwang and J.-W. Park, *Biomedicines*, 2023, **11**, 356.

57 S. Ben Aissa, M. Mastouri, G. Catanante, N. Raouafi and J. L. Marty, *Antibiotics*, 2020, **9**, 860.

58 M. Mastouri, S. Baachaoui, A. Mosbah and N. Raouafi, *RSC Adv.*, 2022, **12**, 13003–13013.

59 J. Santos, T. Castro, A. Venâncio and C. Silva, *Heliyon*, 2023, **9**, e19921.

60 Y. Xie, L. A. Eriksson and R. Zhang, *Nucleic Acids Res.*, 2020, **48**, 6471–6480.

61 F. A. Azri, J. Selamat, R. Sukor, N. A. Yusof, N. H. A. Raston, S. Eissa, M. Zourob and R. Chinnappan, *Anal. Bioanal. Chem.*, 2021, **413**, 3861–3872.